Available online at www.sciencedirect.com

ScienceDirect

Advances in Space Research 74 (2024) 3011–3027

ADVANCES IN SPACE RESEARCH (a COSPAR publication)

www.elsevier.com/locate/asr

Long-term analysis of Sentinel-6A orbit determination: Insights from three years of flight data

Daniel Calliess [a,b], Oliver Montenbruck [a,*], Martin Wermuth [a], Heinz Reichinger [c]

[a] Deutsches Zentrum für Luft- und Raumfahrt (DLR), German Space Operations Center (GSOC), Münchener Straße 20, 82234 Weßling, Germany
[b] Delft University of Technology, Faculty of Aerospace Engineering, Delft, the Netherlands
[c] Beyond Gravity, 1120 Vienna, Austria

Received 22 March 2024; received in revised form 15 June 2024; accepted 17 June 2024
Available online 20 June 2024

Abstract

The Sentinel-6A mission extends the set of satellites dedicated to continuous ocean altimetry measurements, which started with TOPEX/Poseidon in 1992. To utilize these measurements, high-accuracy orbit solutions with radial position errors of less than 1.5cm (RMS) are required. For precise orbit determination (POD), a dedicated GPS/Galileo triple-frequency receiver (PODRIX) is available. Complementary to this, the TriG receiver provides GPS-only observations for POD and radio occultations. Previous research has shown that reduced-dynamic orbit solutions with PODRIX GPS/Galileo measurements meet the mission requirement for radial position accuracy of 1.5 cm (RMS). However, baseline estimation between the PODRIX and TriG antennas still reveals obvious inconsistencies in the along- and cross-track directions. In this study, we present a comprehensive reprocessing of orbit solutions using three years of Sentinel-6A flight data from both receivers covering January 2021 to December 2023. Cross-comparison between both receivers shows that inconsistencies can be removed by applying a yaw bias and a timing error correction. A comparative analysis of macro-models demonstrates strong correlation of cross-track empirical accelerations with the Sun elevation above the orbital plane when using nominal surface properties reported by the manufacturer. Adjusted macro-models improve performance at the expense of requiring increased surface areas or reflectivity coefficients. In addition to improved radiation pressure models, newly estimated antenna patterns and a time-varying gravity field were used in the analysis. The reprocessed data confirm good agreement of the results of both receivers except for a relative timing error of 1.3 μs, and the yaw bias correction of $-0.43°$ removes previously-observed systematic differences in the estimated empirical accelerations. Satellite laser ranging results based on SLRF2020 station coordinates demonstrate a 5—6 mm (1D RMS) accuracy of the GNSS-based POD solutions across the IGb14/IGS20 reference frame transition in November 2022.

Keywords: Sentinel-6A; POD; GNSS; PODRIX; TriG; Orbit determination; Satellite macro-model

1. Introduction

Copernicus is an Earth Observation program established by the European Union (EU) to provide policymakers and public authorities with valuable information on our planet such as sea level rise. The Sentinel-6 mission, as part of Copernicus, focuses on the extension to three decades of mean sea level measurements and sea state data, initially collected with TOPEX/Poseidon since 1992 and followed by the Jason satellite missions (Fu et al., 1994; Ménard et al., 2003; Lambin et al., 2010; Vaze et al., 2010). Next to that, other operational data such as wave height for marine applications is made available in near real-time (Donlon et al., 2021). Sea level change is a key indicator

* Corresponding author.
E-mail addresses: D.L.Calliess@student.tudelft.nl (D. Calliess), oliver.montenbruck@dlr.de (O. Montenbruck), martin.wermuth@dlr.de (M. Wermuth), heinz.reichinger@beyondgravity.com (H. Reichinger).

https://doi.org/10.1016/j.asr.2024.06.043
0273-1177/

to assess climate change and is used by organizations like the International Panel for Climate Change (IPCC).

Sentinel-6A, named Michael Freilich and launched in November 2020, is the first of two identical altimetry satellites, with Sentinel-6B planned for launch in 2026. The orbit is the same as that of its predecessors, a circular orbit at 1336 km altitude with 66° inclination and period of 112 min repeating its ground track every 9.92 days. The main payload for altimetry comprises a dual-frequency Ku/C-band nadir-pointing synthetic aperture radar altimeter (Poseidon-4). This is complemented by the Advanced Microwave Radiometer-Climate (AMR-C) instrument, the Radiation Environment Monitor (REM), and the TriG GPS receiver (Young, 2017) for radio occultation and precise orbit determination (POD). For POD, Sentinel-6A, furthermore, carries a redundant pair of GPS/Galileo (PODRIX) receivers, along with a Laser Retroreflector Array (LRA) for satellite laser ranging (SLR), and a Doppler Orbitography Radio-positioning Integrated by Satellite (DORIS) system (Donlon et al., 2021).

Since sea level measurements are derived from radar range observations and the satellite altitude, precise knowledge of the satellite orbit is fundamental. The Sentinel-6A POD mission requirements demand a non-time-critical (NTC) radial position accuracy of 1.5 cm or better, with the goal being 1 cm (Donlon et al., 2021). Previous research has already proven excellent performance of GNSS-based POD solutions using the dual-constellation PODRIX receiver. Montenbruck et al. (2021) demonstrate that with 6 months of early flight data, GPS-only and Galileo-only ambiguity-fixed reduced-dynamic orbit solutions are consistent to 1 cm (3D RMS) with dual constellation GPS/Galileo solutions. These dual-constellation orbits achieve a 6 mm standard deviation of satellite laser ranging (SLR) residuals. This is confirmed by the European Space Agency (ESA), presenting dual-constellation orbits with SLR residuals below 1.5 cm RMS for more than 95 % of days over 1.5 years of flight data (Zandbergen et al., 2022). A similar performance is reported by Peter et al. (2022) with flight data from 2021. Galileo-only tracking is better in terms of measurement errors and ambiguity fixing statistics than GPS-only, however the combination of both outperforms single constellation products due to the increased number of available satellites (Montenbruck et al., 2021; Zandbergen et al., 2022; Peter et al., 2022). For modeling of solar radiation pressure (SRP) forces on Sentinel-6A, different macro-models with up to 12 panels are used in previous POD studies (Conrad et al., 2022; Cerri et al., 2023; Montenbruck et al., 2021), which represent modified versions of the manufacturer model described in (Cullen, 2023). As an alternative to macro-models, the utilization of a ray-tracing model is presented in Zandbergen et al. (2022), which accounts for self-shadowing based on a more refined computer aided design (CAD) model of the Sentinel-6A spacecraft. While the ray-tracing model is reported to provide a better consistency with the observed orbital dynamics than alternative macro-models considered in that work, details of the ray-tracing model are not presently available to the public for independent validation.

Within the Copernicus Precise Orbit Determination (CPOD; Fernandez et al., 2024) quality working group (QWG), Sentinel-6A POD solutions are routinely generated by a total of 11 analysis centers using different sensors (GNSS, DORIS, SLR), POD tools, and processing standards. These are later combined into a weighted average orbit solution, serving as a reference orbit for comparison and quality control (GMV, 2024; Fernandez et al., 2024). The individual orbit products are mainly based on PODRIX GNSS observations and exhibit consistency at the 2–6 mm in radial direction and 0.3–3 cm in 3D position. Orbits based on TriG observations should agree with the above mentioned PODRIX-derived solutions, however baseline estimations between both receivers revealed obvious deviations in along-track (≈9 mm) and cross-track direction (≈14 mm) (Desai et al., 2022; Montenbruck et al., 2022b). A yaw bias correction of −0.43 ° (Desai et al., 2022; Montenbruck et al., 2022b) was therefore adopted by the CPOD Service and QWG starting in 2023. Sentinel-6A attitude modelling is also addressed in Jin et al. (2023), albeit with lacking access to measured attitude data. In the absence of measured attitude quaternions, Jin et al. (2023) aimed to infer the attitude control law based on the analysis of GNSS-data from the TriG and PODRIX GPS receivers. However, their empirical expressions for the yaw angle variation mask the concept of the actual yaw steering law and hide the presence of the yaw bias mentioned above.

The present study complements previous research on Sentinel-6A POD with a comprehensive reprocessing of three years of GNSS observations from the PODRIX and TriG receivers. Following a description of the two instruments and the available data sets in Section 2, the estimation of antenna baseline corrections from a differential carrier phase processing is presented in Section 3. It confirms the need for a yaw-bias correction of Sentinel-6A attitude quaternions as a prerequisite for the subsequent precise orbit determination. An overview of general POD models and GNSS processing standards used in this study is provided in Section 4, while Section 5 assesses the performance of different macro-models for solar radiation pressure forces. POD results are presented and evaluated in Section 6 using cross-comparisons and SLR analyses. As part of this, the impact of the IGb14/IGS20 reference frame transition in November 2022 on the GNSS-based POD results is assessed and the suitability of SLRF2020 station coordinates for SLR analysis is demonstrated across the entire data period. Finally, a summary and conclusions are presented in Section 7.

2. GNSS instruments and data sets

Sentinel-6A is equipped with a cold-redundant pair of PODRIX receivers built by RUAG Space, now Beyond

Gravity (Peter et al., 2022), in Austria and the TriG receiver (Young, 2017) developed by the Jet Propulsion Laboratory (JPL). All three receivers are operated with a common type of patch excited cup (PEC) choke ring antennas of Beyond Gravity (Öhgren et al., 2011) and differ only in the connector type.

The location and orientation of the three antennas on the top panel of Sentinel-6A is illustrated in Fig. 1. Only the nominal PODRIX and TriG antenna are of interest in this study, since use of the redundant PODRIX receiver and antenna was limited to the commissioning phase. The spacecraft reference frame (SRF) originates at the geometric center of the spacecraft to launcher interface. The x_{sc}-axis marks the nominal flight direction, the z_{sc}-axis points in nadir direction and the y_{sc}-axis completes the orthogonal right-handed system (Cullen, 2023). The antenna reference frames are also indicated in Fig. 1, with the antenna z-axis pointing in opposite direction of the z_{sc}-axis.

A schematic view of the PEC antenna illustrating the location of the frequency-dependent phase centers and the antenna reference point (ARP) is given in Fig. 2. For the present study, phase center offsets (PCOs) relative to the ARP have been derived from pre-flight calibrations provided in the instrument calibration database (Zangerl, 2019) by minimizing the measured phase variations over an off-boresight angle range of $0° \leqslant \theta \leqslant 80°$. Numerical values of the respective PCOs are summarized in Table 1 for each individual antenna unit along with the antenna reference point positions in the SRF. Next to the values for the individual frequency bands, the PCOs for the ionosphere-free L1/L2 and E1/E5a combinations are given, which provide the basis for POD with GPS and Galileo observations. PCO differences between the two antennas are at the 1 mm level with peak values of about 1.4 mm along the y-axis. These differences represent limitations in the repeatability of both the manufacturing process and the factory calibration, but are typically smaller than the impact of the spacecraft environment on the phase center location.

Upon transformation to the adjusted phase centers, the azimuth-averaged phase variations are confined to a range of less than $\pm$ 2 mm up to off-boresight angles of 80° and an even smaller range of about $\pm$ 1mm applies for the ionosphere-free dual-frequency combinations. It should be noted, though, that the phase patterns measured in the pre-flight calibration are not necessarily representative

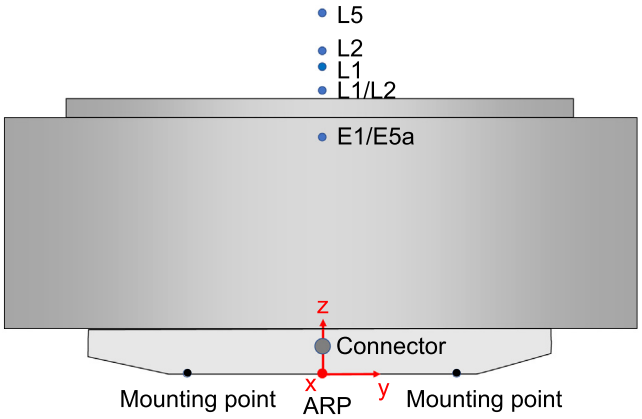

Fig. 2. Schematic view of phase center locations of the PEC GNSS antenna for individual frequencies and ionosphere-free dual-frequency combinations.

Table 1
Antenna reference points ((x, y, z) in SRF) and manufacturer-calibrated phase center offsets ((x, y, z) in antenna reference frame)

Parameter	PODRIX nominal [mm]	TriG [mm]
ARP	(+2474.8, +0.1, −1080.3)	(+600.0, −0.4, −1095.1)
PCO (L1,E1)	(+0.6, +0.6, +96.6)	(−0.2, −0.7, +97.2)
PCO (L2)	(+0.6, +0.7, +101.9)	(−0.1, −0.8, +102.9)
PCO (E5a)	(+0.7, +0.6, +113.7)	(−0.2, −0.8, +114.7)
PCO (L1/L2)	(+0.6, +0.5, +88.4)	(−0.2, −0.7, +88.5)
PCO (E1/E5a)	(+0.6, +0.7, +75.0)	(−0.1, −0.7, +75.2)

of the phase variations encountered after integration of the antenna into the spacecraft. Here, notably larger phase variation may be encountered due to wave-front distortions and multipath caused by the local environment.

The PODRIX receiver of Sentinel-6A is configured for tracking of dual-frequency C/A and L2C signals in the case of GPS IIR-M, IIF and III satellites, while C/A and L1/L2 P(Y)-code signals are tracked for the remaining GPS IIR satellites. It also tracks the E1/E5a signals of the Galileo satellites, making it the first receiver to provide GPS/Galileo observations on a scientific spacecraft in low Earth orbit (LEO). A maximum of 18 satellites can be tracked in total which roughly matches the number of visible GPS and Galileo satellites above the 10° elevation threshold adopted in this mission (Peter et al., 2022). The TriG receiver, in contrast, tracks dual-frequency L1 C/A and

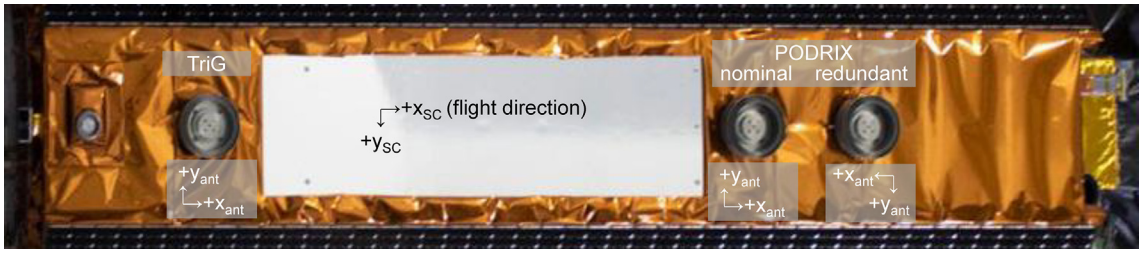

Fig. 1. Top panel of Sentinel-6 spacecraft illustrating the location and orientation of the three GNSS antennas (base image: ESA).

L1/L2 P(Y)-code signals for up to a total of 16 visible GPS satellites (Young, 2017) down to an elevation mask of 0°. This includes 12 satellites for POD observed with the zenith-looking antenna and four satellites for radio-occultation measurements.

Within this study, GNSS measurements covering a period from January 2021 to December 2023 are processed and analyzed. Hourly TriG observation data in the Receiver INdependent EXchange format (RINEX; Romero, 2020) are publicly made available through the Physical Oceanography Distributed Active Archive Data Center (PODAAC; Ocean Surface Topography Science Team, 2021) as part of the Sentinel-6A Level 1B data products, while PODRIX GNSS data and attitude quaternions are shared through the recently opened Copernicus Data Space Ecosystem (CDSE) platform[1].

As an alternative to the public PODRIX data, RINEX files for the present work were generated from the raw receiver telemetry to directly align the receiver time scale with GPS time and to apply receiver-related differential code biases corrections between GPS C/A, P(Y), and L2C signals for improved wide-lane ambiguity resolution (Montenbruck et al., 2021). Furthermore, occasional half-cycle slips caused by phase glitches in the PODRIX frontends for the L1, L2 and L5 frequency bands were removed by checking for apparent clock offset and carrier phase discontinuities in the observation data and applying a corresponding correction to the affected signals of all tracked satellites after the epoch of the cycle-slip. In the case of the TriG receiver, measurements in the public RINEX observation files are referred to a receiver time scale that reflects the natural oscillator drift and gradually deviates from GPS time. To facilitate relative positioning between the two receivers, the TriG observations provided by PODAAC were converted from receiver time to GPS time and subsequently extrapolated to integer GPS seconds using calculated range-rate values. Concerning Sentinel-6A attitude information, the CDSE presently provides unmodified attitude quaternions prior to September 3, 2023 but includes a $-0.43°$ yaw bias correction (see Section 3) from this epoch onwards. For a consistent assessment and handling of attitude information throughout the entire data arc, distinct sets of attitude quaternions with and without yaw-bias correction were therefore derived for the present study.

3. Antenna baseline estimation and attitude modeling

After clock correction and alignment of the TriG measurement epochs to integer GPS seconds, double-differences

$$\phi^{i,j}_{\mathrm{T,P}} = \phi^{i}_{\mathrm{T}} - \phi^{i}_{\mathrm{P}} - \phi^{j}_{\mathrm{T}} + \phi^{j}_{\mathrm{P}} \tag{1}$$

of carrier phase observations for commonly tracked satellites $i \neq j$ and the two receivers (TriG, T, and PODRIX, P) can be formed for GPS observations on the L1 and L2 frequency. These are described by the observation model

$$\lambda\phi^{i,j}_{\mathrm{T,P}} = -\boldsymbol{e}^{i,j} \cdot (\boldsymbol{r}_{\mathrm{PC,T}} - \boldsymbol{r}_{\mathrm{PC,P}} + \boldsymbol{d}) + \xi^{i,j}_{\mathrm{T,P}} + \lambda N^{i,j}_{\mathrm{T,P}}, \tag{2}$$

where, λ denotes the carrier phase wavelength, $\boldsymbol{e}^{i,j}$ is the difference of line-of-sight unit vectors to the tracked GPS satellites, $\boldsymbol{r}_{\mathrm{PC,T}}$ and $\boldsymbol{r}_{\mathrm{PC,P}}$ are the nominal positions of the antenna phase centers, $\xi^{i,j}_{\mathrm{T,P}}$ denotes the double-difference of antenna phase variations, and $N^{i,j}_{\mathrm{T,P}}$ is the double-difference ambiguity. The vector $\boldsymbol{d}$ designates the difference between the true and modeled antenna baseline which is nominally zero and can be determined from (2) on an epoch-by-epoch basis in a least-squares adjustment of observed double-difference carrier phases for the simultaneously tracked satellites. For practical purposes, the observation model is formulated in the spacecraft reference frame, making use of the known spacecraft attitude to obtain the line-of-sight directions relative to the satellite's body axes.

The integer ambiguity in (2) is not known beforehand, but can be determined in a straightforward manner through integer rounding

$$N^{i,j}_{\mathrm{T,P}} = \mathrm{round}\left[\lambda\phi^{i,j}_{\mathrm{T,P}} + \boldsymbol{e}^{i,j} \cdot (\boldsymbol{r}_{\mathrm{PC,T}} - \boldsymbol{r}_{\mathrm{PC,P}})\right] \tag{3}$$

under the provision that the baseline correction and the phase variations are sufficiently small with respect to the wavelength. The double-difference ambiguities for each satellite i are formed relative to a common pivot satellite j and considered as successfully fixed, if their float value differs from the rounded integer value by less than 0.2 cy. Among others, half-cycles ambiguities that mostly affect the TriG data, can be identified and discarded in this way.

Baseline estimates were computed on a daily basis over the three-year interval at 10 s sampling in periods with nominal, forward-looking spacecraft orientation. Independent baseline corrections were computed relative to the ARP, i.e. without considering a priori antenna phase center offsets and patterns in the observation model, as well as using the manufacturer calibrations in Table 1. The averaged baseline corrections $\boldsymbol{d} = (d_x, d_y, d_z)$ in the SRF

Table 2
Statistics of long-term baseline corrections in SRF derived from differential GPS carrier phase observations on L1 and L2 during periods of nominal flight orientation. Individual results are provided for corrections relative to the ARP and considering pre-flight antenna calibrations. For each case, the 3-year median of the daily mean ± the median of the daily standard deviation of epoch-wise baseline estimates are shown.

Solution	d_x [mm]	d_y [mm]	d_z [mm]
TriG-PODRIX L1 (ARP)	9.1 ± 1.9	14.0 ± 1.9	1.6 ± 5.8
TriG-PODRIX L2 (ARP)	9.9 ± 2.8	14.1 ± 2.7	5.3 ± 8.5
TriG-PODRIX L1 (calib)	9.9 ± 1.9	12.6 ± 1.9	1.6 ± 5.9
TriG-PODRIX L2 (calib)	10.7 ± 2.9	12.6 ± 2.7	6.1 ± 8.7

[1] https://dataspace.copernicus.eu/browser; Sentinel-6 Auxiliary Data Files, AUX_GNSSRD (observations) and AUX_PROQUA (quaternions) products.

are shown in Table 2. The results indicate obvious deviations from the a priori baseline in x- and y-direction and an inconsistency between L1/L2 results in the z-direction.

The offset in y-direction can best be understood as a yaw-bias in the attitude telemetry and control of Sentinel-6A, as first suggested in Desai et al. (2022) and Montenbruck et al. (2022b). Fig. 3 illustrates the impact of an attitude error in yaw-direction on the modelled antenna positions. Nominal attitude quaternions are reported by the onboard star sensors and used by the attitude control system, but the spacecraft body itself is slightly offset in yaw direction, thus rotating the true antenna positions away from the x-axis. At the Trig–PODRIX antenna separation of 1875 mm in flight direction, the 14 mm y-difference between the measured baseline and the nominal antenna baseline obtained under the assumption of identical antenna phase center offsets and patterns corresponds to a $-0.43°$ yaw-angle offset. A slightly smaller offset of $-0.39°$ is obtained when considering the manufacturer calibrations. However, it remains unclear to what extent these calibrations are representative of the antenna characteristics after spacecraft integration. A $-0.43°$ yaw-angle correction has therefore been recommended for Sentinel-6A POD by the CPOD service and will gradually be implemented in the operational and reprocessed CPOD products. The same value has also been adopted for this study and is used for the POD solutions discussed in Section 4.

Other than the purely geometrical y-offset, the ≈10 mm deviation in x-direction is of a different nature and best explained by a relative timing error between both receivers, which translates into an along-track position error in proportion to the spacecraft velocity. This is evidenced by the fact that the estimated x-component of the baseline correction in the SRF experiences a sign change whenever the Sentinel-6A spacecraft is flying in reverse orientation. By way of example, Fig. 4 shows the baseline correction for July 1, 2021 during which the satellite underwent a yaw-flip maneuver rotating the spacecraft by 180° about the z-axis.

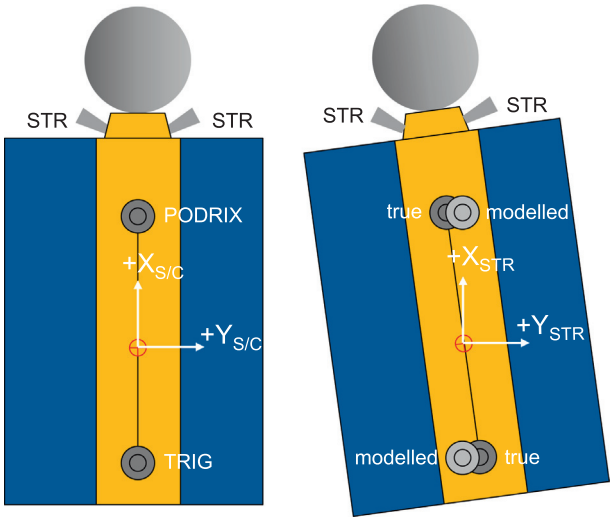

Fig. 3. Impact of a yaw bias due to alignment offsets between the body frame as realized by the star tracker (STR) and the mechanical spacecraft frame as represented by the modelled antenna positions. Schematic views of the nominally aligned configuration (left) and the actual Sentinel-6A configuration (right).

In total, Sentinel-6A was flying in a reversed orientation for five periods of about 3–4 days during periods of low Sun elevation above the orbital plane (β-angle) in 2021 and 2022. By comparing the baseline estimates for periods of nominal and reversed flight directions, the relative along-track shift can be isolated from contributions of the antenna location. Almost identical values of 9.0 mm and 9.2 mm are obtained for L1 and L2, respectively, which indicates a common timing offset of about 1.3 μs at the given orbital velocity of 7.2 km/s. Similar microsecond-level timing offsets have previously been reported in signal simulator tests of other spaceborne GNSS receivers (Montenbruck et al., 2006) and can, for example, be attributed to timing differences in the latching of code and carrier measurements (Sleewaegen et al., 2012) or uncorrected code biases at the few-hundred-meter level. In the absence of suitable pre-flight calibrations, it is not presently possible to unambiguously attribute the observed timing bias to either of the receivers. Some further indications may, however, be obtained from the analysis of satellite laser ranging observations, which suggest a joint contribution from both the TriG and PODRIX receivers (Section 6).

Concerning the z-component of the estimated baseline correction, it appears tempting to infer a small pitch bias in analogy with the yaw offset discussed above. Care must be taken, though, that notably different results are obtained in this case from differential carrier phase observations on the L1 and L2 frequency. As such, the observed d_z values are likely to result from phase pattern distortions and local multipath that affect the PODRIX and TriG antennas in a different manner. No pitch bias is therefore assumed in the subsequent POD solutions of Sentinel-6A.

4. Precise orbit determination

Precise orbits are generated using DLR's GNSS High precision Orbit determination Software Tools (GHOST; Wermuth et al., 2010), covering 1095 days from January 2021 to December 2023. The reduced-dynamic approach is used, combining a dynamical trajectory model of Sentinel-6A with GNSS observations (Wu et al., 1991). A batch least-squares estimation technique is used to determine the epoch-wise state vector, receiver clock offset, inter-system bias, carrier phase ambiguities and empirical accelerations. The latter are estimated as piecewise constant accelerations in 10 min intervals in radial, tangential and normal directions to account for remaining deficiencies in the model. An overview of the adopted parameters and models for POD is provided in Table 3.

The dynamical model employs a time-varying Earth gravity field, Sun and Moon perturbations, relativistic

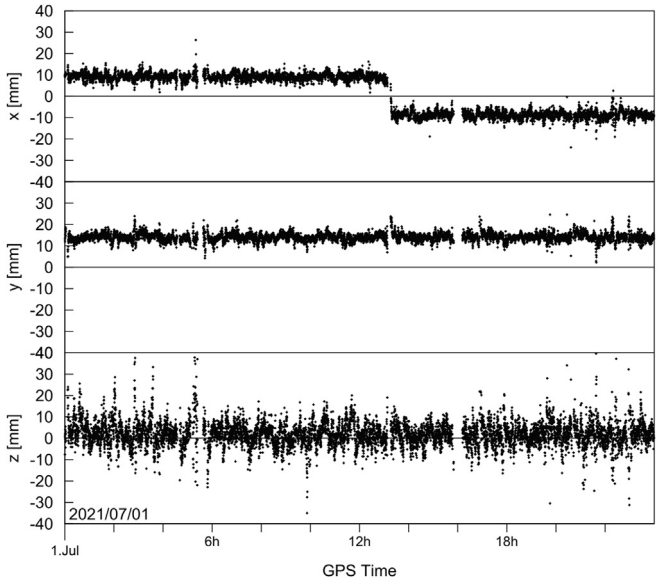

Fig. 4. Baseline corrections (in SRF) from differential L1 carrier phase measurements on 2021/07/01 (DOY 182), showing the impact of a yaw-flip.

corrections (Schwarzschild terms), and a macro-model for drag and radiation pressure forces (Section 5). Earth albedo and infrared radiation are included following the concept of Knocke et al. (1988). Compared to the original model, we make use of a higher resolution grid of 15 rings and 135 sectors for the Earth surface visible from the satellite as well as a newly derived set of polynomial/harmonic coefficients for approximating the latitudinal and seasonal variation of albedo and emissivity based on monthly CERES ES-4 maps (Hackel, 2019). Ocean tides are computed from the FES2004-TEG4 model (Lyard et al., 2021). Precise GNSS orbits, clocks, and accompanying signal-specific phase/code biases are available from the Center for Orbit Determination in Europe (CODE) as part of the International GNSS Service (IGS; Johnston et al., 2017). The processing is split into two phases, where CODM rapid products are employed during applicability of the IGb14 reference frame and CODOPSFIN final products along with IGS20 since GPS week 2238 (November 27, 2022). The IGS antenna models were linearly extrapolated beyond off-boresight angles of 14–15° for Galileo in-orbit-validation (IOV) satellites and extended from 14–17° for GPS block III satellites as described in Conrad et al. (2023). Improved receiver antenna phase centers were estimated for IGb14/IGS20, as explained in Section 6.1.

A yaw angle correction of −0.43° has been applied to the measured attitude quaternions. Spacecraft-related information including antenna and center-of-mass positions, surface data, mass and maneuver information are obtained from (Cullen, 2023) and the mission operations team.

Carrier phase integer ambiguities are resolved with a single-receiver wide-lane/narrow-lane technique described in Montenbruck et al. (2018), where observations are processed in passes with constant ambiguities. The Hatch-Melbourne-Wuebbena combination (HMW) (Hatch, 1983; Melbourne, 1985; Wübbena, 1985) is calculated for each pass and corrected with fractional satellite-specific wide-lane biases. The common fractional wide-lane bias of the receiver can be isolated by differencing between passes and integer rounding. The resulting wide-lane integer ambiguity is then combined with float-valued carrier phase range biases estimated for each pass. Finally, integer rounding of between-pass differences is used to find the L1 integer ambiguities.

5. Solar radiation pressure modeling

The dynamical trajectory model employs a macro-model to estimate non-gravitational forces such as solar and Earth radiation pressure. The macro-model simplifies the spacecraft structure into a collection of flat plates, and the net radiation pressure force per surface element can be calculated according to Milani et al. (1987).

Four different macro-models are compared in this study, comprising a DLR 8-panel configuration (Montenbruck et al., 2021), the original 12-panel manufacturer model (Cullen, 2023), a 6-panel box-wing model by CNES recommended for DORIS processing (Cerri et al., 2023) and the 12-panel macro-model of (Conrad et al., 2022) with adjusted surface areas, referred to as UoC/JPL (University of Colorado and Jet Propulsion Laboratory) model. Table 4 summarizes the normal vectors, surface areas and optical surface properties of these models, including the fractions of absorbed, diffusely-reflected and specularly-reflected photons in the visible and infrared spectrum.

The specific shape of Sentinel-6A causes shadowing of the lower body by the solar panels depending on the Sun incidence angle. The effects of self-shadowing are difficult to handle in a macro-model approach and consistently neglected in all models considered here. A rigorous treatment requires a full ray-tracing model as discussed in (Zandbergen et al., 2022), but was unavailable for this study.

Following Cerri et al. (2010), spontaneous and diffuse re-emission of absorbed photons should be considered for all surfaces covered with multi-layer insulation for thermal protection purposes. Surfaces with assumed re-emission in the DLR, CNES and manufacturer models are indicated by an asterisk (*) in Table 4. The model by Conrad et al. (2022) does not assume re-emission and instead adjusts the effective surfaces areas as part of the POD process. This can lead to unrealistically large surface areas as seen in Table 4. Concerning the DLR model, we note that spontaneous re-emission is also considered for the solar panels. While this lacks an adequate physical motivation, the model retains the nominal surface areas and is ultimately justified by a good agreement of modelled and observed accelerations.

Fig. 5 shows the resulting empirical accelerations in cross-track direction based on orbit solutions with all four

Table 3
Models and parameters used for Sentinel-6A precise orbit determination

Model/Parameter	Description	
Estimation technique	Batch least squares estimation with single receiver ambiguity resolution (Montenbruck et al., 2018)	
GNSS observations	Undifferenced dual-frequency phase and pseudorange; 24h daily arcs, 30s sampling[a,b]	
Reference Frame	IGb14 (up to day 2022/330) (Rebischung, 2020)	IGS20 (from 2022/331) (Villiger, 2022)
GNSS orbit and clock data	CODM rapid solutions (30s sampling) (Dach et al., 2020)	COD0OPSFIN final solutions (30s sampling) (Dach et al., 2023)
GNSS code and phase biases	CODM rapid biases for GPS/Galileo (Dach et al., 2020)	COD0OPSFIN final biases for GPS/Galileo (Dach et al., 2023)
GNSS satellite antennas	igs14.atx with IOV extension to 15° and GPS III extension (Conrad et al., 2023)	igs20.atx with GPS III extension (Conrad et al., 2023)
Receiver	PODRIX	TriG
Observation types	GPS modernized: C1C L1C C2L L2L, GPS legacy: C1W L1C C2W L2W, Galileo: C1C L1C C5Q L5Q	GPS: C1W L1C C2W L2W
S6A antennas	POD (nominal) In-flight PCO + PV calibrations for IGb14 and IGS20 periods	POD-RO In-flight PCO + PV calibrations for IGb14 and IGS20 periods
S6A attitude	Quaternions (measured)[c], -0.43° yaw bias correction	
Phase windup	modelled (Wu et al., 1993)	
Earth gravity	GOCO06S truncated at degree and order 70 (Kvas et al., 2021)	
Third body effects	Sun and Moon point-mass model; analytical series of luni-solar coordinates (Montenbruck and Pfleger, 2000)	
Ocean tides	FES2004-TEG4 (Lyard et al., 2006)	
Solar radiation pressure	Macromodel, see Table 4	
Earth albedo and IR radiation	Knocke et al. (1988) formulation with CERES Earth radiation data (Priestley et al., 2011)	
Earth orientation parameters	IGS rapid series (IGS0OPSRAP)[d]	
Empirical accelerations	Piecewise constant accelerations	
Estimation parameters	Epoch-wise clock offsets and inter-system biases Epoch state (position, velocity) Piecewise constant accelerations in RTN frame with 600s intervals constrained to 4/8/8 nm/s^2 Carrier phase ambiguities (one per continuous carrier phase tracking arc)	

[a] https://dataspace.copernicus.eu/browser; Sentinel-6 Auxiliary Data Files, AUX_GNSSRD (observations)
[b] Ocean Surface Topography Science Team (2021)
[c] https://dataspace.copernicus.eu/browser; Sentinel-6 Auxiliary Data Files, AUX_PROQUA (quaternions) products.
[d] https://igs.org/products-access/earth-rotation

macro-models. The magnitude of empirical accelerations and their correlation with the Sun elevation angle above the orbit frame (β) provide a good indication of the quality of the macro-model. The original manufacturer model and the CNES model suffer from strong correlation with the β-angle, while the empirical accelerations estimated with the DLR and UoC/JPL models are essentially free of seasonal variations. Both these models clearly improve the performance compared to the original manufacturer data. However, this improvement comes at the expense of either increased re-emission contributions or increased surface areas that do not correspond to the real spacecraft geometry.

Previously, a systematic bias of around 8 nm/s^2 in the cross-track empirical accelerations was observed in the Sentinel-6A POD of Montenbruck et al. (2021). This bias has essentially vanished after implementation of the yaw bias correction in the POD results of both receivers, as illustrated in Fig. 6 for the TriG based results. The radial and tangential directions exhibit near-zero empirical accelerations, while small dips at high β-angles remain in the tangential direction. This is likely due to remaining deficiencies in the non-gravitational force models, specifically the lacking consideration of the aforementioned self-shadowing and thermal radiation effects.

6. POD performance and validation

For further analysis, independent POD solutions based on processing of PODRIX and TriG data were computed for the 3-year analysis period based on the general processing standards described in Table 3. More specifically, the DLR macro-model was adopted for non-gravitational force modeling (see Section 5) and the −0.43° yaw bias correction discussed in Section 3 was applied.

6.1. Antenna characterization

In a first step, improved estimates of the effective antenna phase center offsets in boresight (i.e., z-) direction were obtained by minimizing the radial offset between reduced-dynamic and kinematic position solutions. In view

Table 4
Sentinel-6A macro-model surface definitions and optical parameters (fractions α, δ, and ρ of absorbed, diffusely reflected and specularly reflected photons for visual (VIS) and infrared (IR) radiation), for four different models: DLR, DORIS, Conrad and original manufacturer model (Montenbruck et al., 2021; Cerri et al., 2023; Conrad et al., 2022; Cullen, 2023). The surface normal vectors are defined in the SRF, surfaces including spontaneous re-emission (R) of photons are denoted with *.

Model	Element	Surface normal	Area [m^2]	α_{VIS}	δ_{VIS}	ρ_{VIS}	α_{IR}	δ_{IR}	ρ_{IR}	R
DLR	Body $+X$ (front)	$(+1.000, +0.000, +0.000)$	3.5	0.47	0.04	0.49	0.76	0.04	0.20	*
	Body $-X$ (back)	$(-1.000, +0.000, +0.000)$	3.5	0.43	0.12	0.45	0.78	0.04	0.18	*
	Body $+Z$ (bottom)	$(+0.000, +0.000, +1.000)$	15.5	0.57	0.08	0.35	0.77	0.12	0.11	*
	Body $-Z$ (top)	$(+0.000, +0.000, -1.000)$	2.0	0.35	0.03	0.62	0.77	0.01	0.22	*
	Solar panel (starboard)	$(+0.000, +0.616, -0.788)$	8.9	0.86	0.14	0.00	0.80	0.20	0.00	*
	Solar panel (portside)	$(+0.000, -0.616, -0.788)$	8.9	0.86	0.14	0.00	0.80	0.20	0.00	*
	Body $+Y$ (bottom structures)	$(+0.000, +1.000, +0.000)$	1.0	0.43	0.14	0.43	0.75	0.12	0.13	*
	Body $-Y$ (bottom structures)	$(+0.000, -1.000, +0.000)$	1.0	0.43	0.14	0.43	0.75	0.12	0.13	*
DORIS	Body $+X$ (front)	$(+1.000, +0.000, +0.000)$	3.37	0.00	0.541	0.459	0.00	0.808	0.192	*
	Body $-X$ (back)	$(-1.000, +0.000, +0.000)$	3.6	0.43	0.12	0.45	0.78	0.04	0.18	*
	Body $+Z$ (bottom)	$(+0.000, +0.000, +1.000)$	15.35	0.028	0.63	0.342	0.21	0.724	0.066	*
	Body $-Z$ (top)	$(+0.000, +0.000, -1.000)$	2.99	0.034	0.511	0.455	0.259	0.627	0.114	*
	Solar panel (starboard)	$(+0.000, +0.616, -0.788)$	8.66	0.663	0.337	0.00	0.385	0.615	0.00	
	Solar panel (portside)	$(+0.000, -0.616, -0.788)$	8.66	0.663	0.337	0.00	0.385	0.615	0.00	
Manufacturer	Body $+X$ (front)	$(+1.000, +0.000, +0.000)$	2.99	0.46	0.04	0.50	0.46	0.04	0.50	*
	Body $-X$ (back)	$(-1.000, +0.000, +0.000)$	3.35	0.46	0.04	0.50	0.46	0.04	0.50	*
	Body $+Z$ (bottom)	$(+0.000, +0.000, +1.000)$	9.03	0.38	0.02	0.60	0.38	0.02	0.60	*
	Body $-Z$ (top)	$(+0.000, +0.000, -1.000)$	1.80	0.32	0.03	0.65	0.32	0.03	0.65	*
	Solar panel top (starboard)	$(+0.000, +0.616, -0.788)$	8.65	0.86	0.14	0.00	0.86	0.14	0.00	
	Solar panel top (portside)	$(+0.000, -0.616, -0.788)$	8.65	0.86	0.14	0.00	0.86	0.14	0.00	
	Solar panel bottom (starboard)	$(+0.000, +0.616, +0.788)$	4.09	0.84	0.16	0.00	0.84	0.16	0.00	
	Solar panel bottom (portside)	$(+0.000, -0.616, +0.788)$	4.09	0.84	0.16	0.00	0.84	0.16	0.00	
	Body $+Y$ (starboard)	$(+0.000, +1.000, +0.000)$	2.87	0.46	0.04	0.50	0.46	0.04	0.50	*
	Body $-Y$ (portside)	$(+0.000, -1.000, +0.000)$	2.87	0.46	0.04	0.50	0.46	0.04	0.50	*
	AMR-C top	$(+0.469, +0.000, -0.833)$	0.92	0.92	0.08	0.00	0.92	0.08	0.00	
	AMR-C bottom	$(-0.469, +0.000, +0.833)$	0.92	0.25	0.56	0.19	0.25	0.56	0.19	
Conrad	Body $+X$ (front)	$(+1.000, +0.000, +0.000)$	4.149	0.61	0.041	0.349	0.61	0.041	0.349	
	Body $-X$ (back)	$(-1.000, +0.000, +0.000)$	3.941	0.412	0.042	0.546	0.412	0.042	0.546	
	Body $+Z$ (bottom)	$(+0.000, +0.000, +1.000)$	11.83	0.413	0.016	0.571	0.413	0.016	0.571	
	Body $-Z$ (top)	$(+0.000, +0.000, -1.000)$	2.072	0.31	0.03	0.66	0.31	0.03	0.66	
	Solar panel top (starboard)	$(+0.000, +0.616, -0.788)$	8.65	0.545	0.316	0.139	0.545	0.316	0.139	
	Solar panel top (portside)	$(+0.000, -0.616, -0.788)$	8.65	0.545	0.316	0.139	0.545	0.316	0.139	
	Solar panel bottom (starboard)	$(+0.000, +0.616, +0.788)$	3.76	0.823	0.164	0.013	0.823	0.164	0.013	
	Solar panel bottom (portside)	$(+0.000, -0.616, +0.788)$	3.76	0.823	0.164	0.013	0.823	0.164	0.013	
	Body $+Y$ (starboard)	$(+0.000, +1.000, +0.000)$	1.329	0.454	0.04	0.506	0.454	0.04	0.506	
	Body $-Y$ (portside)	$(+0.000, -1.000, +0.000)$	1.329	0.454	0.04	0.506	0.454	0.04	0.506	
	AMR-C top	$(+0.469, +0.000, -0.833)$	0.92	0.92	0.08	0.00	0.92	0.08	0.00	
	AMR-C bottom	$(+0.000, +0.000, +1.000)$	0.8123	0.25	0.56	0.19	0.25	0.56	0.19	

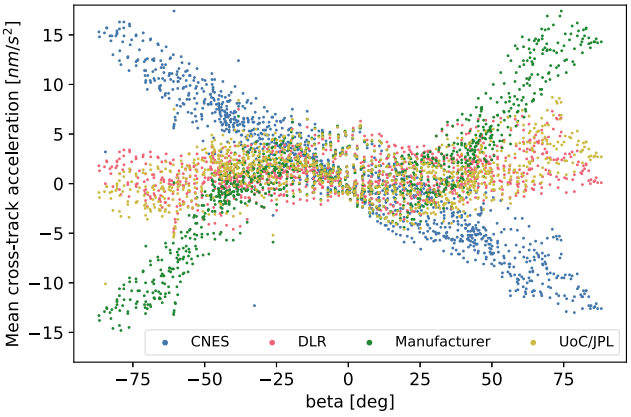

Fig. 5. Daily mean values of estimated empirical accelerations in cross-track direction plotted against the Sun elevation β above the orbital plane for the DLR, CNES, UoC/JPL and manufacturer macro-models.

of the transition of the IGS reference frame and the associated GNSS antenna models from IGb14/igs14.atx to IGS20/igs20.atx at the beginning of GPS week 2238 (Nov 27, 2022), independent z-PCOs were derived for use with the old and new conventions. Given the partly incomplete IGS antenna models for large off-boresight angles, the patterns of the Galileo in-orbit validation (IOV) satellites in igs14.atx were linearly extrapolated from 14° to 15°. In the case of GPS III, the phase pattern extension model of Conrad et al. (2023) for off-boresight angles of 14–17° was applied instead of the constant values in igs14.atx and igs20.atx.

The results in Table 5 confirm a good consistency of the two antennas, but also notable differences with respect to the manufacturer (see Table 1). Part of these can be understood by the inconsistency of GPS and Galileo transmit antenna calibrations in the igs14.atx antenna model, but discrepancies at the 10 mm level can still be observed when working with the self-consistent igs20.atx model. The 3–4 mm increase of the GPS-related PCOs reflects an adjustment of the terrestrial reference frame scale of roughly +0.5ppb in the IGb14 to IGS20 transition, which is accompanied by an average change of the GPS transmit antenna z-PCOs of the IGS antenna model by −67 mm. For Galileo satellites, in contrast, igs14.atx made use of manufacturer calibrations, which are incompatible with the IGb14 scale and required a +156 mm change for igs20.atx to achieve consistent GPS and Galileo station heights in the IGS20 reference frame. This causes a predicted decrease of Galileo-based stations heights by approximately 6 mm (Montenbruck et al., 2022a) in good accord with the PCO shifts in Table 1. Use of the igs20.atx antenna model instead of the igs14.atx one yields a clearly improved consistency of the observed Sentinel-6A L1/L2 and E1/E5a phase centers, even though their relative location is still inverted compared to the factory calibrations. It is presently unclear, whether and to which extent the apparent discrepancy of pre-flight and in-flight PCO calibrations can be explained by the impact of the spacecraft environment or relate to differences in the elevation-dependent distribution of factory calibration grid points as compared to the true observations.

Maps of phase variations obtained from L1/L2 and E1/E5a carrier phase residuals relative to the adjusted phase centers are shown in Fig. 7 for the two operational receivers and antennas. Compared to the factory calibrations of the standalone antennas, the in-flight calibrations show pronounced variations with patchy large-scale structures and superimposed fringes that indicate the presence of multipath effects. From the orientation and separation of the fringes, a subtle cross-talk, i.e., interference between signals from the radio occultation and POD antenna branches in the TriG receiver, may be suspected, which was earlier encountered in the CHAMP and GRACE missions (Montenbruck and Kroes, 2003; Mao et al., 2017). On the other hand, similar fringe patterns with a slightly wider spacing can be recognized in the PODRIX phase maps. In view of a widely different receiver design and the fact that only a single antenna is used in the PODRIX receiver these patterns cannot be explained by self-interference. However, it may be noted that cross-talk from amplified signals of a TriG precursor to another onboard GPS receiver has previously been reported in Montenbruck et al. (2008). It remains unclear at this point, whether a similar leakage occurs in the TriG receiver and explains the interference patterns observed in the carrier phase observations of the PODRIX receiver on Sentinel-6A.

6.2. Measurement quality

The overall measurement quality and goodness of fit of the respective observations are characterized by the residuals statistics in Table 6. Phase residuals are obtained after consideration of in-flight phase pattern calibration and are thus largely freed from local multipath errors. In the case of the PODRIX receiver, tracking of the modernized civil GPS signals (L1 C/A, L2C) shows a better quality than the semi-codeless P(Y) code tracking, but both are outperformed by the Galileo measurements. TriG code observations show roughly similar code residuals as the PODRIX P(Y) pseudoranges, but reduced carrier phase errors.

Considering the fact that the ionosphere-free measurement combination results in a roughly threefold noise level compared to that of the individual observations, representative RMS code errors of 0.10–0.25 m can be inferred, while individual phase measurements exhibit RMS errors at the 1.5 mm level.

The code and phase measurement errors directly affect the quality of the Hatch-Melbourne-Wuebbena combination, which is used for fixing of the wide-lane ambiguities. Again, Galileo tracking yields a clearly better performance with RMS errors of about 0.1 m (or 0.1 cy) for epoch-wise HMW observations, while GPS observations result in roughly two times larger values for both receiver types.

The distribution of daily ambiguity fixing rates, as measured by the ratio of tracking passes with fixed ambiguities

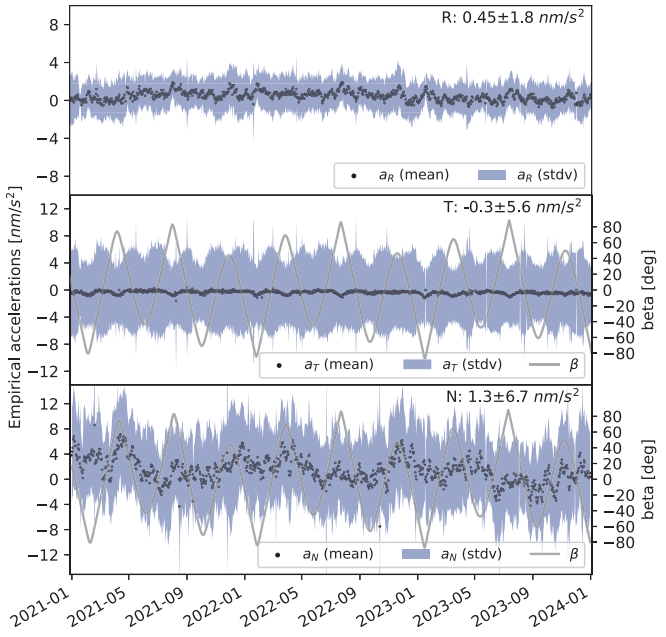

Fig. 6. Daily mean values (black) and 1-σ bounds (light blue) of estimated empirical accelerations in radial (top), along-track (center), and cross-track (bottom) direction for TriG POD results (Section 3) with adopted yaw bias of. −0.43°. (For interpretation of the references to colour in this figure legend, the reader is referred to the web version of this article.)

and the total number of passes, is illustrated in Fig. 8 for the three-year data analysis period. Wide-lane ambiguities in a combined GPS/Galileo orbit determination could be fixed with median success rates of 98.8% and 99.9% for GPS and Galileo tracking, respectively. TriG data, in contrast, exhibit a large number of half-cycle ambiguities, which reduce the wide-lane fixing rate to a median value of 91.7%. The N_1 narrow-lane ambiguities could be fixed with success rates of 97.9% and 99.6% in PODRIX POD solutions and 77.8% in the TriG processing.

6.3. Orbit comparison

For an initial performance assessment, the POD solutions generated in this study are compared against the combined orbit products (COMB) of the CPOD service (GMV, 2024; Fernandez et al., 2024). The latter are obtained from a weighted average of individual analysis centers (ACs) with weights based on the median position offset relative to the arithmetic mean of all centers. The combination process reduces the contribution of random errors in the individual solution and thus improves the overall precision. Given the diversity of processing standards and the use of partly different observations techniques (GNSS, DORIS, SLR), the averaging of AC-specific systematic errors may likewise contribute to an overall accuracy improvement.

Since the AC contributions to the COMB solution were initially based on uncorrected attitude quaternions (see Section 3), a systematic lateral position offset can be

Table 5
Estimated phase center offsets from Sentinel-6A GNSS observations. All values in mm.

Antenna	Signals	z_{PCO}	
		igs14.atx	igs20.atx
PODRIX nominal	GPS L1/L2	68	72
	Galileo E1/E5a	90	85
TriG	GPS L1/L2	70	73

observed prior to 2023 in the COMB solution relative to solutions that are obtained with the corrected attitude information. Given the predominant share of PODRIX-based GNSS orbit determination solutions in the combined solution, a cross-track correction of −7.1 mm was therefore applied to the COMB product for the 2021–2022 period for the subsequent analysis. This correction reflects the mismodeling of the PODRIX antenna position in the spacecraft frame for a yaw angle error of −0.43° at the 0.945 m x-offset between the antenna and the center-of-mass (COM). Subject to an ambiguity-fixed processing and a reduced-dynamic orbit determination approach, the attitude mismodeling results in a corresponding shift of the estimated COM position in the POD. Even though the correction would not apply for highly dynamic solutions as well as DORIS, SLR and TriG-based POD results of Sentinel-6A, their contribution to the COMB product is less pronounced and a good overall performance of the correction is independently evidenced by the SLR analysis described in Section 6.4.

Orbit differences relative to the combined CPOD product were evaluated for different PODRIX- and TriG-based POD solutions computed in the present study. For a harmonized comparison, a −9 mm along-track correction has been applied to the TriG orbits to compensate for the relative timing error discussed in Section 3. Statistics of the daily RMS position errors over the 3-years analysis period are illustrated in Fig. 9 in the form of violin plots with markers for the median values and interquartile ranges. With median 3D RMS difference of 5 mm, both the TriG GPS-only and the PODRIX GPS + Galileo solutions exhibit a high level of consistency with the COMB reference. While the PODRIX results show an even slightly lower peak of the distribution than the TriG solutions, an obvious tail in the probability density may be recognized that demonstrates a non-negligible fraction of daily orbit products with 3D RMS differences of up to 15 mm. The occurrence of large errors is even more pronounced for the single-constellation GPS-only and Galileo-only solutions that exhibit a clearly lower precision.

Closer inspection of PODRIX solutions on days with degraded overall performance shows that the respective solutions are affected by intervals of typically 1 h duration, or half an orbital revolution, during which peak errors in the range of 3–8 cm may be reached. By way of example, this is illustrated in Fig. 10 for a single day in April 2023.

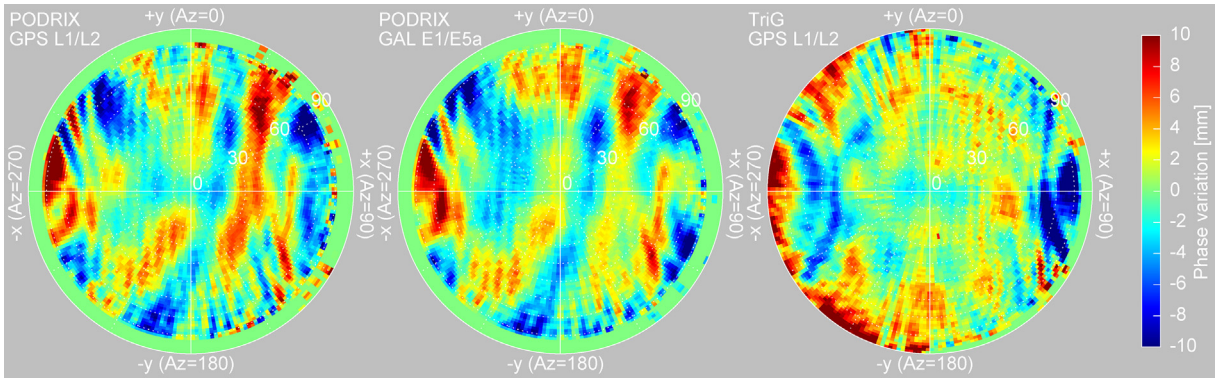

Fig. 7. PCO-free phase variations of the nominal PODRIX antenna and the TriG antenna of Sentinel-6A based on residuals of dual-frequency carrier phase observations.

These errors can best be attributed to false narrow-lane ambiguity fixes that are more likely when the float ambiguities estimated in the initial stage of the reduced-dynamic orbit determination are only poorly determined in the current POD scheme. Even though the TriG solutions exhibit a notably lower overall fixing rate, they benefit from a larger number of concurrently tracked GPS satellites and increased overlap of tracking arcs within an individual constellation. More specifically, an average of 9.1 GPS satellites is tracked and used for POD at each epoch in case of the TriG receiver, while 7.4 GPS and 6.0 Galileo satellites are processed on average in the PODRIX POD. Further investigation will be required to improve the robustness of the ambiguity fixing in the present POD system software used within this study and to investigate the compatibility of the PODRIX observations with the employed ambiguity resolution strategy.

6.4. SLR analysis

Sentinel-6A is routinely tracked by roughly 30 SLR stations of the International Satellite Laser Ranging Service (ILRS; Pearlman et al., 2019). Complementary to the orbit comparison discussed above, the evaluation of SLR residuals enables an independent accuracy analysis of the GNSS-based POD solutions relative to an external reference.

In view of notable differences in the quality of SLR measurements from individual stations, the analysis is intentionally limited to 17 high performance stations (Arequipa 7403, Grasse 7845, Graz 7839, Greenbelt 7105, Haleakala 7119, Hartebeesthoek 7501, Herstmonceaux 7840, Matera 7941, Monument Peak 7110, Mount Stromlo 7825, Papeete 7124, Potsdam 7841, Simosato 7838, Wettzell 7827, Wettzell 8834, Wuhan 7396, and Yarragadee 7090) with RMS residuals of less than 10 mm and a 6 mm median of the station-wise RMS residuals in the period of interest. These provide a total of about 270000 normal points, making up about 75% of the overall Sentinel-6A tracking data collected by the ILRS from 2021 to 2023.

Satellite laser ranging provides the turn-around time of photons transmitted by the SLR station and received again after reflection at the satellite. Upon multiplication of the semi-duration with the speed of light a "1-way" range is obtained that provides an approximate measure of the geometric station-to-satellite distance. SLR residuals, i.e., differences between the measured ranges and modelled values computed from the known spacecraft orbit, provide a figure of merit for the accuracy of the respective orbit product. Fundamental algorithms for modeling SLR observations of LEO satellites considering the varying station-to-satellite geometry during the signal propagation are described in Arnold et al. (2019). Aside from the trajectory of the tracked satellite as well as the location and optical properties of the laser retro-reflector array (LRA), the computation of modelled ranges takes into account time-dependent station coordinates, atmospheric range delays, range biases and the relativistic space–time curvature correction. Specific models used in the Sentinel-6A analysis are summarized in Table 7. Note that no use was made of range biases in the SLRF2020 Data Handling File, since the respective values are based on spherical satellites and not well adapted to work with LEO satellites. Instead,

Table 6
Median values of daily RMS pseudorange and carrier phase residuals in PODRIX and TriG orbit determination. All values refer to ionosphere-free combination of dual-frequency observations as identified by the respective RINEX (Romero, 2020) signal codes.

Measurement	PODRIX			TriG
	GPS 1C/2L	GPS 1 W/2 W	GAL 1C/5Q	GPS 1 W/2 W
Pseudorange [m]	0.56	0.75	0.37	0.71
Carrier phase [mm]	4.6	4.8	3.9	4.4

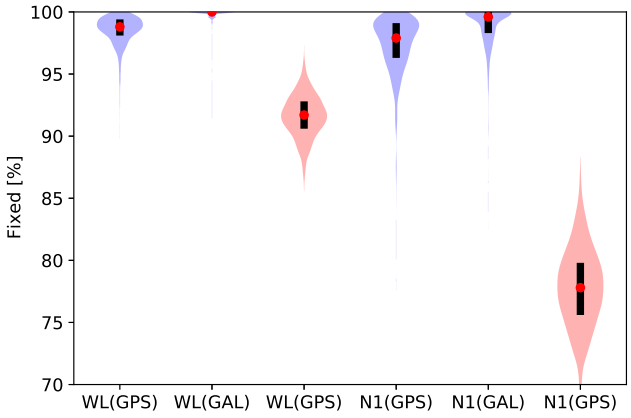

Fig. 8. Distribution of wide-lane (left) and N_1 ambiguity fixing rates (right) from daily POD solutions for 2021–2023. Results for the PODRIX receiver (blue) refer to a combined GPS/Galileo solution, while TriG results (red) are exclusively based on GPS tracking. Median values are indicated by red dots, while black bars show the inter-quartile range. (For interpretation of the references to colour in this figure legend, the reader is referred to the web version of this article.)

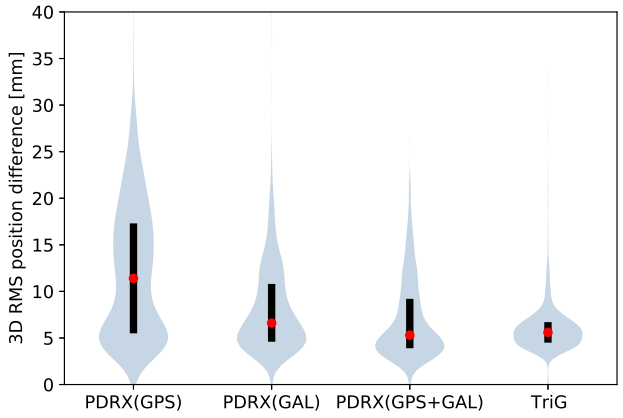

Fig. 9. Distribution of daily 3D RMS position differences of PODRIX- and TriG-based POD solutions with respect to the CPOD combined solution. A −9 mm along-track correction has been applied to all TRIG solutions to compensate the relative measurement time offset between both receivers. Furthermore, a −7.1 mm cross-track offset has been applied to the COMB orbits for 2021 and 2022 to compensate for the lacking yaw angle correction in CPOD analysis center products used for the generation of the combined orbit product. Median values are indicated by red dots, while black bars show the inter-quartile range. (For interpretation of the references to colour in this figure legend, the reader is referred to the web version of this article.)

range biases were independently adjusted from the Sentinel-6A observations as discussed below.

Along with the residuals, we compute the partial derivatives of the modeled ranges with respect to range biases, station coordinate corrections, and LRA position offsets. These are used for an optional adjustment of observation model parameters based on a least-squares minimization of the SLR residuals (Arnold et al., 2019). Four distinct processing approaches are distinguished, which differ by the types of parameters adjusted from the SLR residuals. Aside from the station-specific ranging biases, which are well recognized as systematic error sources in the modeling of SLR observations (Saquet et al., 2024; Strugarek et al., 2021; Arnold et al., 2019), we consider corrections to the adopted LRA position in the spacecraft frame as well as corrections to the individual SLR station positions. When adjusting multiple types of parameters from the difference of observed and modeled SLR ranges, the range biases and LRA or station position offsets decorrelate due to the varying line-of-sight geometry, provided that observations over a sufficiently large elevation range are considered. On the other hand, a near-degeneracy arises when jointly estimating corrections of the LRA z-position and station heights due to the nadir looking orientation of the Sentinel-6A spacecraft. Therefore, only the x- (along-track) and y- (cross-track) component of the LRA were adjusted simultaneously with the estimation of station coordinate corrections. For the Sentinel-6A orbit analysis, the individual parameters are estimated as constant values over the entire 3-year data arc and can be freely adjusted from the observations.

SLR station positions in our study are consistently modeled based on SLRF2020 coordinates and ITRF2020 post-seismic deformations (PSDs) throughout the entire 3-year period. While this raises an apparent inconsistency with the use of IGb14 GNSS orbit and clock products for Sentinel-6A orbit determination until November 2022, SLRF2020 offers clearly improved consistency with the IGb14-aligned Sentinel-6A orbits than SLRF2014 with ITRF2014 PSDs (ILRS, 2020a; ITRF, 2020). By way of example, SLR residuals of PODRIX POD solutions for January 2021 to November 2022 obtained with station-specific range bias corrections decrease from 8.0 mm to 7.1 mm (RMS) when working with SLRF2020 rather than the (presumably IGb14-compatible) SLRF2014 frame. Likewise, station coordinate corrections relative to SLRF2020 derived from IGb14-referenced Sentinel-6A orbits using the methodology described in Arnold et al. (2019) are systematically lower than those relative to SLRF2014 as illustrated in Fig. 11.

Station coordinates used for the computation of SLR residuals are corrected for atmospheric pressure loading (APL) using precomputed values from the Vienna Mapping Function (VMF) Open Access Data server (VMF,

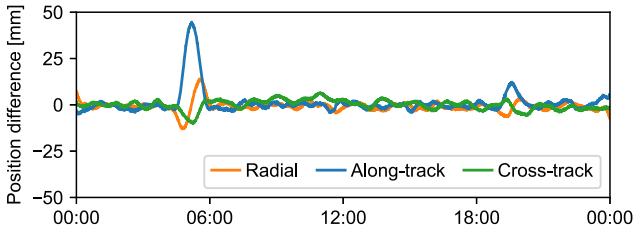

Fig. 10. Position differences of PODRIX-based GPS + Galileo orbit determination and COMB reference for April 10, 2023 indicating the impact of false ambiguity fixes.

2021). Despite these site-specific corrections, seasonal variations with mostly annual period and amplitudes at the few-mm level can be discerned in residuals time series of various SLR stations (e.g., Greenbelt, Potsdam). The actual nature of these variations is not presently known and may relate to seasonal range bias variations, tropospheric modeling issues, or unmodelled hydrological loading. For comparison, similar variations remain when using the ITRF2020 seasonal harmonics models (Altamimi et al., 2023) instead of APL corrections, even though APL modeling yields slightly reduced overall residuals for the affected stations.

The overall performance of the various POD solutions for the three-year analysis period is summarized in Table 8 for PODRIX and TriG solutions obtained in this study as well as the combined CPOD solution. Station-specific range bias corrections and SLRF2020 station coordinate offsets estimated from the Sentinel-6A SLR residuals exhibit representative magnitudes of 1–10 mm and peak values of about 2.5 cm with formal errors at the 0.5 mm level. If uncorrected, RMS residuals of roughly 9 mm are obtained for the three solutions. Adjustment of range bias, LRA and station position corrections, in contrast, reduces the residuals to a level of 5–6 mm and enables a sharper discrimination of the solution quality (Table 8). Again, best results are obtained for the COMB product, followed by the TriG- and PODRIX-based orbits with 10–20% higher residuals.

The SLR residuals of Table 8 obtained without adjustment of range biases or other parameters provide direct evidence for a better than 1 cm (1D RMS) accuracy of the Sentinel-6A POD solutions. An even two times better performance is indicated by the residuals obtained after the estimation and correction of range biases, station coordinates and LRA offsets. While some orbit errors might, in principal, be absorbed in these parameters, the impact appears negligible in the present context, since only a single parameter set is adjusted from the entire three-year data arc. As such orbit errors and the adjusted SLR model parameters are essentially uncorrelated and the resulting residuals are considered to provide a realistic measure of the achieved orbit accuracy.

Further insight into the orbit determination accuracy may be obtained from the estimated LRA offsets relative to the nominal mounting position. The corresponding results collated in Table 9 indicate consistency at the 1 mm between the observed and modeled LRA offset from the center-of-mass in spacecraft z- and y-directions, but notable systematic, solution-specific offsets of up to 5 mm in magnitude in the $+x$-direction. As discussed before, such offsets can readily be understood by subtle timing errors in the GNSS measurements that show up in systematic along-track position errors. Based on the analysis of differential carrier phase measurements, a 9 mm or 1.3 μs offset between the TriG and PODRIX receivers has previously been derived in Section 3, which likewise shows up in the comparison of LRA x-corrections for the two receivers. Inspection of the individual values indicates that both receivers exhibit similar offsets of 4–5 mm or 0.5–0.7 μs, albeit with opposite signs, relative to the SLR reference. This differs from early analyses of Desai et al. (2022) that attributed most of the differential timing offset exclusively to the TriG receiver. It should be noted, though, that the use of SLR as an absolute reference is itself subject to possible timing biases in the SLR network as well as uncertainties in the modeled LRA location relative to the COM.

Concerning the estimated z-corrections, an excellent agreement between the observed and modeled height of Sentinel-6A is evidenced for all three orbit products. More specifically, the analysis shows a high level of overall consistency between the center-of-mass altitude as constrained by orbital dynamics models in the POD, the modeled LRA position relative to the spacecraft COM, and the mean height of the SLR station network in the SLRF2020 frame. Despite this encouraging result, care must be taken that individual uncertainties are likely to be much larger than 1 mm and the good agreement obtained in the present cases may be partly coincidental. By way of example, systematic height differences of up to ± 3 mm relative to the COMB solution have been identified for Sentinel-6A products of individual analysis centers in GMV (2024), which reflect systematic differences in radial acceleration models such as Earth radiation pressure. Similar uncertainties are likely to apply for the actual knowledge of the COM location relative to the spacecraft structure.

Time series of SLR residuals for the individual solutions are shown in Fig. 12. None of the graphs exhibits systematic variations in the residuals related to the β-angles, i.e., the Sun's elevations above the orbital plane of the Sentinel-6A spacecraft, which indicates a high-fidelity modeling of solar radiation pressure in each of the three orbit products. As already shown in Table 8, the lowest overall residuals are obtained for the combined solution (COMB) of the Copernicus POD Service. At an RMS value of 5.2 mm, the COMB orbits show only sparse cases of residuals in the range of 20–60 mm. Correlated outliers at the respective epochs can be recognized in the other solutions, thus indicating erroneous SLR measurements rather than the orbit products in these cases. In contrast to this, the higher level of increased residuals of the GNSS-based POD results computed in the present study evidences a partly degraded quality of these orbit products. This is most obvious for the PODRIX solutions, which likely suffer from an increased frequency of false ambiguity fixes (see Section 6.3) in our solutions.

7. Summary and conclusions

The co-location of two GNSS receivers with DORIS and an SLR reflector onboard the Sentinel-6A spacecraft offers a unique opportunity to assess the quality of LEO precise orbit determination and the consistency of different space geodetic techniques. Sentinel-6A thus provides an important test bed for the preparation of the GENESIS

Table 7
Models and data sets for Sentinel-6A SLR validation

Station coordinates	SLRF2020 (ILRS, 2020b) and ITRF2020 PSDs (Altamimi et al., 2023; ITRF, 2022)
Solid Earth and pole tides	IERS2003 (McCarthy and Petit, 2004)
Ocean tide loading	FES2014b (Lyard et al., 2021)
Atmospheric pressure loading	TU Vienna model (Wijaya et al., 2013; VMF, 2021)
Tropospheric refraction	IERS2010 (Petit and Luzum, 2010), Mendes and Pavlis (2004)
Relativity	Space–time curvature correction applied
LRA optical center	$(+1.6248, -0.4006, +0.6648)$ m
LRA range correction	Azimuth- and nadir-angle-dependent correction computed from design information in (Desai and Zohar, 2020)
Outlier screening	10cm, 99.74th percentile

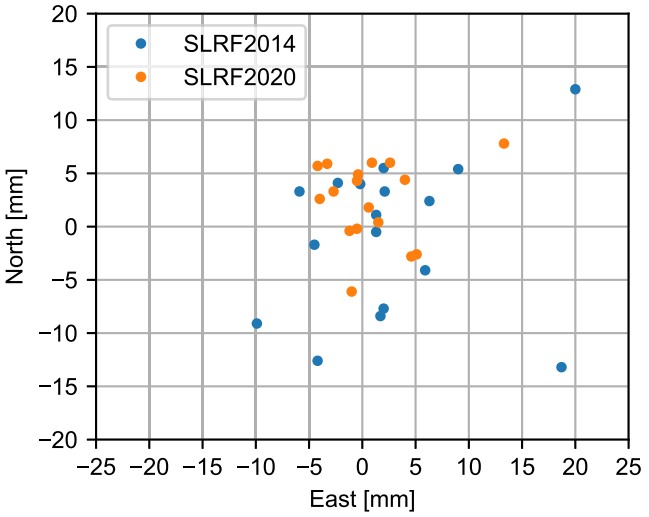

Fig. 11. SLRF2014 and SLRF2020 horizontal station coordinate adjustments derived from SLR residuals of PODRIX-based Sentinel-6A orbits for 17 high performance stations. RMS values amount to 10 mm and 6 mm, respectively.

mission (Delva et al., 2023; Ventura-Traveset, 2022; Montenbruck et al., 2023), which aims to improve the International Terrestrial Reference Frame (ITRF) based on co-located GNSS, SLR, DORIS, and VLBI instruments on a satellite in medium altitude Earth orbit.

Within the present study, focus is given to the improvement of observation models and dynamical models as well as the comparison of POD solutions from observations of the TriG GPS-only receiver and the dual-constellation PODRIX receiver over a three-year period from January 2021 to December 2023. Based on the analysis of differential carrier phase measurements from both receivers, a $-0.43°$ yaw bias in the reported spacecraft attitude and a 1.3 μs relative timing error between PODRIX and TriG GNSS observations are inferred. Upon correction of the yaw offset, systematic cross-track biases between the respective POD solutions as well as the estimated cross-track accelerations are removed. For the modeling of non-gravitational forces, in particular solar radiation pressure, the performance of different macro-models is evaluated. Systematic deviations between modeled and observed accelerations are evidenced for a macro-model based on the manufacturer-provided satellite geometry and optical surface parameters, while best results (i.e., reduced correlation between estimated empirical accelerations and β angle) are obtained in empirically calibrated models assuming either increased surface areas or increased re-radiation. The root cause of this apparent discrepancy is not presently known, and the present findings clearly indicate a need for more detailed investigations of self-shading effects and thermal radiation budgets in the non-gravitational force modeling of this spacecraft.

Table 8
Satellite laser ranging residuals of PODRIX GPS/Galileo and TriG POD solutions as well as the combined CPOD solution for the 2001–2023 period in the SLRF2020 frame. RMS values in mm. COMB solutions prior to 2023 have been corrected with a cross-track offset of -7.1mm to account for the lacking yaw angle correction in the underlying CPOD analysis center products.

Adjusted	PODRIX	TriG	COMB
none	9.4	8.8	8.6
range bias	7.1	6.3	6.1
LRA(x, y, z), range bias	6.7	6.0	5.7
LRA(x, y), pos, range bias	6.3	5.6	5.2

Given the transition of the GNSS- and SLR-based terrestrial reference frames to IGS20 and SLRF2020 during the 3-year analysis period, special attention is given to the impact of this change on observation modeling and orbit determination. Concerning GNSS, the use of the new, IGS20-compatible igs20.atx transmit antenna model offers a notably improved consistency of observed and factory-calibrated GPS and Galileo phase center offsets for the receiving antennas of Sentinel-6A rather than the old igs14.atx model. Nevertheless, inconsistencies at the 10 mm level remain, which hint at possible phase center shifts upon integration of the antenna into the spacecraft. While knowledge of the phase center-location is vital for purely kinematic POD, the orbital height in a dynamically

Table 9
LRA offset corrections from adjustment of LRA offsets and range biases (A) and from adjustment of LRA offsets, range biases and station position offsets (B). All values in mm. COMB solutions prior to 2023 have been corrected with a cross-track offset of -7.1mm to account for the lacking yaw angle correction in the underlying CPOD analysis center products.

Solution	A			B		
	x	y	z	x	y	z
PODRIX	+5.1	+0.2	−0.9	+5.1	−0.5	–
TriG	−3.9	+0.5	−0.8	−3.9	−0.3	–
COMB	+4.8	−1.0	−1.0	+4.7	−1.2	–

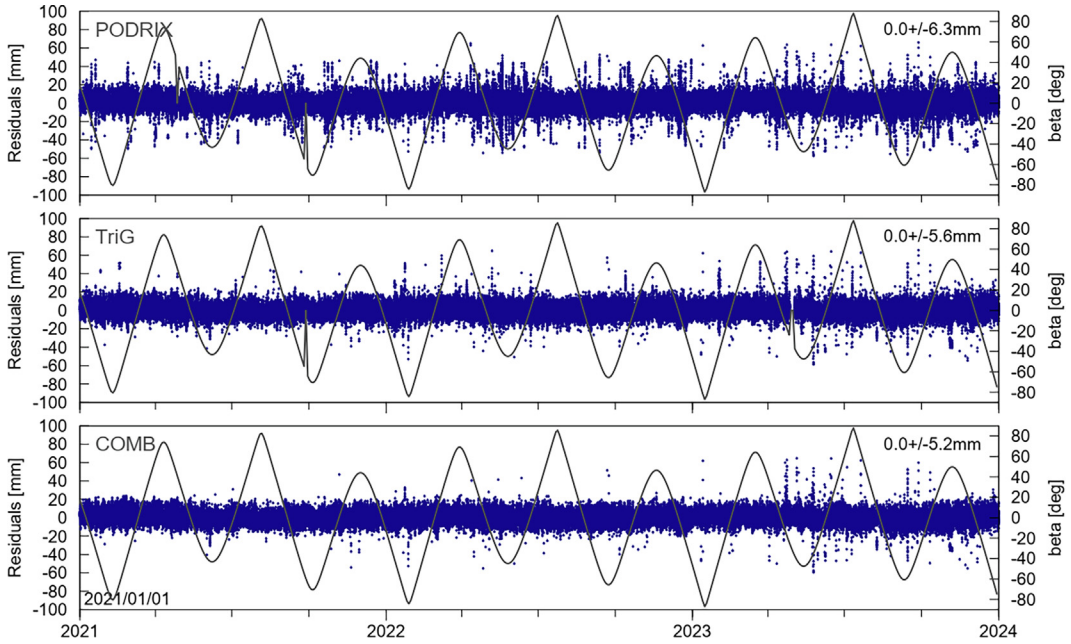

Fig. 12. SLR residuals of the PODRIX (top), TriG (center), and combined CPOD (bottom) POD solutions of Sentinel-6A over the 3-year analysis period after the adjustment of range biases, LRA offsets, and station position corrections. Values in the top right of each subplot denote mean values ± standard deviations for the individual cases. Gray lines describe the variation of the Sun elevation β over the orbital plane.

constrained POD is largely unaffected by the frame transition and mainly driven by the choice of dynamical models.

The comparison of GNSS-based Sentinel-6A orbit products with satellite laser ranging observations from 17 high-performance stations evidences a sub-centimeter orbit accuracy but likewise indicates various systematic errors in the GNSS observations and the SLR processing. Use of SLRF2020 stations coordinates in the SLR modeling provides notably decreased SLR residuals compared to SLRF2014 throughout the entire analysis period, but still requires adjustment of systematic range biases for best performance and suggests inconsistencies in the adopted station positions of 1–10 mm for individual sites. Concerning the relative timing bias of the TriG and PODRIX receivers, the SLR analysis suggests almost equal contributions of opposite sign from both instruments relative to the time base of the ITRF network.

Overall, the analysis of Sentinel-6A GNSS and SLR observations indicates a persistent need for refined modeling and instrument calibration in order to improve the consistency of different space-geodetic techniques. With respect to GENESIS, timing biases introducing along-track position errors deserve specific attention in addition to the well-known aspects of phase center and center-of-mass determination.

Declaration of Competing Interest

The authors declare that they have no known competing financial interests or personal relationships that could have appeared to influence the work reported in this paper.

Acknowledgments

The authors gratefully acknowledge the provision of Sentinel-6A GNSS observations by the United States' National Air and Space Administration (NASA) and the Copernicus Earth observation component of the European Union's (EU) Space program, as well as the collection and sharing of satellite laser ranging measurements through the International Laser Ranging Service (ILRS). Auxiliary products for the Sentinel-6A data analysis have been provided by the International GNSS Service (IGS) and the Center for Orbit Determination in Europe (CODE). Reference orbits of Sentinel-6A have been provided by the Copernicus POD (CPOD) Service and its Quality Working Group (QWG). Beyond Gravity has contributed to a better understanding of their GNSS antennas and receiver through valuable technical discussions and information. The support of all institutions and individuals is likewise acknowledged.

References

Altamimi, Z., Rebischung, P., Collilieux, X., et al., 2023. ITRF2020: an augmented reference frame refining the modeling of nonlinear station motions. J. Geodesy 97 (5), 47. https://doi.org/10.1007/s00190-023-01738-w.

Arnold, D., Montenbruck, O., Hackel, S., et al., 2019. Satellite laser ranging to low Earth orbiters: orbit and network validation. J. Geodesy 93 (11), 2315–2334. https://doi.org/10.1007/s00190-018-1140-4.

Cerri, L., Berthias, J., Bertiger, W., et al., 2010. Precision orbit determination standards for the Jason series of altimeter missions. Marine Geod. 33 (S1), 379–418. https://doi.org/10.1080/01490419.2010.488966.

Cerri, L., Couhert, A., Ferrage, P., 2023. DORIS satellites models implemented in POE processing, SALP-NT-BORD-OP-16137-CN, v1.18, 26 June 20223. https://ids-doris.org/documents/BC/satellites/DORISSatelliteModels.pdf.

Conrad, A., Axelrad, P., Desai, S. et al. (2022). Improved modeling of the solar radiation pressure for the Sentinel-6 MF spacecraft. In: Proceedings of the 35th International Technical Meeting of the Satellite Division of The Institute of Navigation (ION GNSS+ 2022) (pp. 3618–3631). https://doi.org/10.33012/2022.18478.

Conrad, A., Desai, S., Haines, B., et al., 2023. Extending the GPS IIIA antenna calibration for precise orbit determination of low Earth orbit satellites. J. Geodesy 97 (4), 35. https://doi.org/10.1007/s00190-023-01718-0.

Cullen, R. (2023). Sentinel-6A POD context, JC-TN-ESA-0420, v2.2, 3 May 2023. https://ids-doris.org/documents/BC/satellites/Sentinel6A_PODcontext.pdf.

Dach, R., Schaer, S., Arnold, D. et al., 2023. CODE final product series for the IGS. http://www.aiub.unibe.ch/download/CODE. https://doi.org/10.48350/185744.

Dach, R., Schaer, S., Arnold, D. et al., 2020. CODE rapid product series for the IGS. http://www.aiub.unibe.ch/download/CODE. https://doi.org/10.7892/boris.75854.4.

Delva, P., Altamimi, Z., Blazquez, A., et al., 2023. GENESIS: co-location of geodetic techniques in space. Earth, Planets and Space 75 (1), 5. https://doi.org/10.1186/s40623-022-01752-w.

Desai, S., Conrad, A., Haines, B., 2022. GPS-based precise orbit determination of the Sentinel-6 MF mission. Proceedings of Ocean Surface Topography Science Team meeting. https://doi.org/10.24400/527896/a03-2022.3432.

Desai, S., Zohar, G., 2020. Sentinel-6A LRA information for ILRS, 20 March 2020. https://ilrs.gsfc.nasa.gov/docs/2020/JPL_Inputs_for_ILRS_Mission_Support.pdf.

Donlon, C.J., Cullen, R., Giulicchi, L., et al., 2021. The Copernicus Sentinel-6 mission: Enhanced continuity of satellite sea level measurements from space. Remote Sens. Environ. 258, 112395. https://doi.org/10.1016/j.rse.2021.112395.

Fernandez, J., Peter, H., Fernandez, C., et al., 2024. The Copernicus POD service. Adv. Space Res. https://doi.org/10.1016/j.asr.2024.02.056.

Fu, L.-L., Christensen, E.J., Yamarone Jr, C.A., et al., 1994. TOPEX/POSEIDON mission overview. J. Geophys. Res.: Oceans 99 (C12), 24369–24381. https://doi.org/10.1029/94JC01761.

GMV (2024). Copernicus POD Regular Service Review Jan–Dec 2023, GMV-CPOD3-RSR-0030.

Hackel, S., 2019. Refinement of Reduced-Dynamic Orbit Determination for Low Earth Satellites Ph.D. thesis. Technische Universität München.

Hatch, R., 1983. The synergism of GPS code and carrier measurements. In: International geodetic symposium on satellite Doppler positioning (pp. 1213–1231). volume 2.

ILRS, 2020a. SLRF2014 station coordinates. https://cddis.nasa.gov/archive/slr/products/resource/SLRF2014_POS+VEL_2030.0_200428.snx.

ILRS, 2020b. SLRF2020 station coordinates. https://cddis.nasa.gov/archive/slr/products/resource/SLRF2020_POS+VEL_2023.10.02.snx.

ITRF, 2020. ITRF2014 post-seismic deformation data for SLR stations. ftp://itrf-ftp.ign.fr/pub/itrf/itrf2014/ITRF2014-psd-slr.dat.

ITRF, 2022. ITRF2014 post-seismic deformation data for SLR stations. ftp://itrf-ftp.ign.fr/pub/itrf/itrf2020/ITRF2020-psd-slr.snx.

Jin, B., Chen, S., Li, M., et al., 2023. Sentinel-6A attitude modeling with dual GNSS antennas and its impact on precise orbit determination. GPS Solutions 27 (1), 7. https://doi.org/10.1007/s10291-022-01346-9.

Johnston, G., Riddell, A., Hausler, G., 2017. The International GNSS Service. In: Teunissen, P., Montenbruck, O. (Eds.), Springer Handbook of Global Navigation Satellite Systems chapter, 33. Springer, pp. 967–982. https://doi.org/10.1007/978-3-319-42928-1_33.

Knocke, P.C., Ries, J.C., Tapley, B.D., 1988. Earth radiation pressure effects on satellites. In: In AIAA/AAS Astrodynamics Conference, pp. 577–587. https://doi.org/10.2514/6.1988-4292.

Kvas, A., Brockmann, J.M., Krauss, S., et al., 2021. GOCO06s – a satellite-only global gravity field model. Earth Syst. Sci. Data 13 (1), 99–118. https://doi.org/10.5194/essd-13-99-2021.

Lambin, J., Morrow, R., Fu, L.-L., et al., 2010. The OSTM/Jason-2 mission. Mar. Geodesy 33 (S1), 4–25. https://doi.org/10.1080/01490419.2010.491030.

Lyard, F., Lefevre, F., Letellier, T., et al., 2006. Modelling the global ocean tides: modern insights from FES2004. Ocean dynamics 56 (5–6), 394–415. https://doi.org/10.1007/s10236-006-0086-x.

Lyard, F.H., Allain, D.J., Cancet, M., et al., 2021. FES2014 global ocean tide atlas: design and performance. Ocean Sci. 17 (3), 615–649. https://doi.org/10.5194/os-17-615-2021.

Mao, X., Visser, P., Van den IJssel, J., 2017. Impact of GPS antenna phase center and code residual variation maps on orbit and baseline determination of GRACE. Adv. Space Res. 59 (12), 2987–3002. https://doi.org/10.1016/j.asr.2017.03.0.

McCarthy, D.D., Petit, G., 2004. IERS Conventions (2003), Technical Note No. 32. Frankfurt: Bundesamt für Kartographie und Geodäsie.

Melbourne, W., 1985. The case for ranging in GPS based geodetic systems. In: Goad, C. (Ed.), Proc. 1st Int. Symp. on Precise Positioning with the Global Positioning System. NOAA, pp. 373–386.

Ménard, Y., Fu, L.-L., Escudier, P., et al., 2003. The Jason-1 mission special issue: Jason-1 calibration/validation. Mar. Geodesy 26 (3–4), 131–146. https://doi.org/10.1080/714044514.

Mendes, V., Pavlis, E., 2004. High-accuracy zenith delay prediction at optical wavelengths. Geophys. Res. Lett. 31 (14), L14602. https://doi.org/10.1029/2004GL020308.

Milani, A., Nobili, A.M., Farinella, P., 1987. Non-gravitational perturbations and satellite geodesy. Adam Hilger, Bristol.

Montenbruck, O., Garcia-Fernandez, M., Williams, J., 2006. Performance comparison of semicodeless GPS receivers for LEO satellites. GPS Solutions 10, 249–261. https://doi.org/10.1007/s10291-006-0025-9.

Montenbruck, O., Hackel, S., Jäggi, A., 2018. Precise orbit determination of the Sentinel-3A altimetry satellite using ambiguity-fixed GPS carrier phase observations. J. Geodesy 92 (7), 711–726. https://doi.org/10.1007/s00190-017-1090-2.

Montenbruck, O., Hackel, S., Wermuth, M., et al., 2021. Sentinel-6A precise orbit determination using a combined GPS/Galileo receiver. J. Geodesy 95 (9), 109. https://doi.org/10.1007/s00190-021-01563-z.

Montenbruck, O., Kroes, R., 2003. In-flight performance analysis of the CHAMP BlackJack GPS receiver. GPS Solutions 7, 74–86. https://doi.org/10.1007/s10291-003-0055-5.

Montenbruck, O., Pfleger, T., 2000. Astronomy on the personal computer. Springer.

Montenbruck, O., Steigenberger, P., Thoelert, S., et al., 2023. GNSS visibility and performance implications for the GENESIS mission. J. Geodesy 97 (10), 96. https://doi.org/10.1007/s00190-023-01784-4.

Montenbruck, O., Steigenberger, P., Villiger, A., et al., 2022a. On the relation of GNSS phase center offsets and the terrestrial reference frame scale: a semi-analytical analysis. J. Geodesy 96 (11), 90. https://doi.org/10.1007/s00190-022-01678-x.

Montenbruck, O., Wermuth, M., Hackel, S., 2022b. Cross-calibration of the TriG and PODRIX GNSS receivers onboard Sentinel-6A. Proceedings of Ocean Surface Topography Science Team meeting. https://doi.org/10.24400/527896/a03-2022.3307.

Montenbruck, O., Yoon, Y., Ardaens, J.-S. et al. (2008). In-flight performance assessment of the single frequency MosaicGNSS receiver for satellite navigation. In: 7th International ESA Conference on Guidance, Navigation and Control Systems; ESA WPP-288. volume 25.

Ocean Surface Topography Science Team, 2021. Sentinel-6A MF Jason-CS L1B GNSS-RO-POD tracking data hourly. Ver. F, PO.DAAC, CA, USA. https://doi.org/10.5067/S6AGN-1ROPD.

Öhgren, M., Bonnedal, M., Ingvarson, P., 2011. GNSS antenna for precise orbit determination including s/c interference predictions. In: Proc. 5th Europ. Conf. on Antennas and Propagation (EUCAP), pp. 1990–1994.

Pearlman, M.R., Noll, C.E., Pavlis, E.C., et al., 2019. The ILRS: approaching 20 years and planning for the future. J. Geodesy 93 (11), 2161–2180. https://doi.org/10.1007/s00190-019-01241-1.

Peter, H., Springer, T., Zangerl, F., et al., 2022. Beyond gravity PODRIX GNSS Receiver on Sentinel-6 Michael Freilich-Receiver Performance and POD Analysis. In: In Proceedings of ION GNSS+ 2022, pp. 589–601. https://doi.org/10.33012/2022.18368.

Petit, G., Luzum, B., 2010. IERS Conventions (2010), Technical Note No. 36. Frankfurt: Bundesamt für Kartographie und Geodäsie.

Priestley, K.J., Smith, G.L., Thomas, S., et al., 2011. Radiometric performance of the CERES Earth radiation budget climate record sensors on the EOS Aqua and Terra spacecraft through April 2007. J. Atmos. Ocean. Technol. 28 (1), 3–21. https://doi.org/10.1175/2010JTECHA1521.1.

Rebischung, P., 2020. Switch to IGb14 reference frame, IGSMAIL-7921, 14 Apr. 2020. https://lists.igs.org/pipermail/igsmail/2020/007917.html.

Romero, I., 2020. RINEX - the receiver independent exchange format, v. 3.05, 1 December 2020. https://files.igs.org/pub/data/format/rinex305.pdf.

Saquet, E., Couhert, A., Peter, H., et al., 2024. Millimeter accuracy SLR bias determination using independent multi-LEO DORIS and GPS-based precise orbits. Adv. Space Res. 73 (1), 304–316. https://doi.org/10.1016/j.asr.2023.07.014.

Sleewaegen, J.-M., Simsky, A., De Wilde, W., et al., 2012. Demystifying GLONASS inter-frequency carrier phase biases. Inside GNSS 7 (3), 57–61, https://www.insidegnss.com/auto/mayjune12-Sleewaegen.pdf.

Strugarek, D., Sośnica, K., Arnold, D., et al., 2021. Determination of SLR station coordinates based on LEO, LARES, LAGEOS, and Galileo satellites. Earth, Planets and Space 73, 87. https://doi.org/10.1186/s40623-021-01397-1.

Vaze, P., Neeck, S., Bannoura, W. et al., 2010. The Jason-3 Mission: Completing the transition of ocean altimetry from research to operations. In Sensors, systems, and next-generation satellites XIV (pp. 264–268). SPIE volume 7826. https://doi.org/10.1117/12.868543.

Ventura-Traveset, J., 2022. GENESIS: Collocation in space of four geodetic techniques. In: International Committee on GNSS, 9-14 Oct. 2022, Dubai, United Arab Emirates. UNOOSA. https://www.unoosa.org/documents/pdf/icg/2022/ICG16/17.pdf.

Villiger, A., 2022. Upcoming switch to IGS20/igs20.atx and repro3 standards, IGSMAIL-8238, 26 Jul. 2022. https://lists.igs.org/pipermail/igsmail/2022/008234.html.

VMF, 2021. VMF data server. https://doi.org/10.17616/R3RD2H.

Wermuth, M., Montenbruck, O., van Helleputte, T., 2010. GPS high precision orbit determination software tools (GHOST). In: 4th International Conference on Astrodynamics Tools and Techniques.

Wijaya, D.D., Böhm, J., Karbon, M., et al., 2013. Atmospheric pressure loading. In: Atmospheric Effects in Space Geodesy. Springer, pp. 137–157. https://doi.org/10.1007/978-3-642-36932-2_4.

Wu, J.-T., Wu, S.C., Hajj, G., et al., 1993. Effects of antenna orientation on GPS carrier phase. Manuscripta Geodaetica 18 (2), 91–98.

Wu, S.-C., Yunck, T.P., Thornton, C.L., 1991. Reduced-dynamic technique for precise orbit determination of low earth satellites. J. Guid., Control, Dynam. 14 (1), 24–30. https://doi.org/10.2514/3.20600.

Wübbena, G., 1985. Software developments for geodetic positioning with GPS using TI 4100 code and carrier measurements. In: Goad, C. (Ed.), Proc. 1st Int. Symp. on Precise Positioning with the Global Positioning System. NOAA, pp. 403–412.

Young, L., 2017. JPL GNSS receivers, past, present, and future. In SCaN/HEOMD Workshop on Emerging Technologies for Autonomous Space Navigation. NASA. https://hdl.handle.net/2014/47433.

Zandbergen, R., Gini, F., Schönemann, E., et al., 2022. ESA/ESOC-precise orbit determination for Sentinel-6 Michael Freilich based on Galileo and GPS observations. In: Proceedings of ION GNSS+ 2022, pp. 575–588. https://doi.org/10.33012/2022.18413.

Zangerl, F., 2019. PODRIX characterisation and calibration plan; P-11284-PLN-0017-RSA, iss. 6, 27 Nov. 2019.